PERMEABILITY PREDICTION FROM NON-DESTRUCTIVE IMAGING OF COMPOSITE MICROSTRUCTURE

Joy P. Dunkers[1], Frederick R. Phelan[1], Kathleen M. Flynn[1], Daniel P. Sanders[1] and Richard S. Parnas[2]

[1]Polymers Division
National Institute of Standards and Technology
Gaithersburg, MD 20899

[2]Institute of Materials Science
University of Connecticut
Storrs, CT 06269

Abstract

Knowledge of the permeability tensor in liquid composite molding is important for process optimization. Unfortunately, experimental determination of permeability is difficult and time consuming. Numerical calculation of permeability from a model reinforcement can circumvent experimentation. However, permeability predictions often rely on a model reinforcement that does not accurately mimic the actual microstructure. A rapid, non-destructive technique called optical coherence tomography (OCT) can image the microstructure of a composite in minutes. Actual microstructure information can be then used to improve the accuracy of the model and therefore the predicted permeability. Additionally, the influence on fiber volume fraction and microstructural variability on permeability can be systematically studied.

In this work, binary images of the microstructure of a unidirectional E-glass/epoxy composite were generated from the low contrast OCT data through image de-noising, contrast enhancement and feature recognition. The resulting data were input to a lattice Boltzmann model for permeability prediction. Results show that the image processing induced alterations in fiber volume fraction and tow surface area have an influence on the predicted permeability. Level-set methods for image analysis were then used to process the images to binary images. Level-set methods offer image de-noising and feature recognition while preserving fiber volume fraction and tow surface area. The calculated axial and transverse permeabilities from the level-set images shows excellent agreement with experimental values.

Introduction

Fluid flow in Liquid Composite Molding (LCM) processes such as resin transfer molding (RTM) is usually modeled using Darcy's Law given by

$$v = -\frac{\overline{\overline{K}}}{m} \cdot \nabla P \qquad \textbf{(1)}$$

where $\boldsymbol{v}$ is the average (superficial) velocity in the medium, P is the pressure, $\underline{\underline{\boldsymbol{K}}}$ is a symmetric, second order tensor known as the permeability and μ is the fluid viscosity. Darcy's law is a volume-averaged model in which all the complicated interaction that takes place between the fluid and the fiber preform structure is accounted for through the permeability. Accurate permeability data, therefore, are a critical requirement if *a priori* modeling efforts based on Darcy's law are to be successfully used in the design and optimization of these processes. Currently, the most reliable and commonly used technique for obtaining permeability values is via experimental measurements in either radial or uni-directional flow configurations [1]. However, experimental characterization is slow, as it involves a large number of carefully controlled experiments over a large range of volume fractions. Another more serious limitation is that it is difficult to conduct experiments on the materials in the deformed states they encounter when placed in LCM tooling, although there have been some recent efforts [2].

In light of these limitations, computational prediction of permeability [3,4,5] offers a potentially accurate and robust alternative to experimental methods. Such calculations involve imposing a pressure drop across the media, solving the appropriate transport equations for the detailed flow field, and then back-calculating the permeability by applying Darcy's law. The biggest drawback of this approach has been the inability to

accurately determine the detailed geometry of the fibrous preform materials, which in addition to many intricate structural features, typically contain statistical variations and defects in their microstructure [6]. Without a precise representation of the media, it is not possible to accurately predict permeability values using computational methods.

There have been two main approaches to the problem of microstructure determination. The first is to perform calculations on small, computationally efficient "unit cell" structures using nominal dimensions that represent the average preform weave structure. The major problem with this approach is that calculations on the "average" unit cell structure do not in general, yield an accurate value for the average permeability [6]. A second approach is to determine the microstructure via optical methods (e.g., microscopy), and directly perform the numerical calculation on a discretization of the optical image. This approach has the advantage of exactly representing the media, and by including large sections of the media in the image, variations and defects in the microstructure are automatically accounted for in the calculation. However, until recently, this approach was probably even more tedious to perform than direct experimental measurement of permeability since the composite specimens typically had to be carefully sectioned, polished and examined. However, a new technique being investigated in this work called optical coherence tomography (OCT) offers a means for rapidly and non-destructively determining the microstructure of fiber reinforced plastic materials, potentially leading to a robust means of computational permeability prediction.

Optical coherence tomography is a non-invasive, non-contact optical imaging technique that allows the visualization of microstructure within scattering media [7,8,9]. OCT uses light in a manner analogous to the way ultrasound imaging uses sound, providing significantly higher spatial resolution (5 to 20) μm albeit with shallower penetration depth. OCT is based upon low-coherence optical ranging techniques where the optical distance to individual sites within the sample is determined by the difference in time, relative to a reference light beam, for an incident light beam to penetrate and backscatter within the sample. This temporal delay is probed using a fiber optic interferometer and a broadband laser light source. The fiber optic interferometer consists of single-mode optical fiber coupled with a 50/50 fiber optic splitter that illuminates both the sample and a linearly translating reference mirror. Light reflected from the reference mirror recombines with light back-scattered and reflected from the sample at the 50/50 splitter to create a temporal interference pattern which is measured with a photodiode detector. The resulting interference patterns are present only when the optical path difference of the reference arm matches that of the sample arm to within the coherence length of the source. The z axis (Figure 1) spatial resolution that can be obtained with OCT is determined by the coherence length, or inverse spectral width, of the source and is typically (10 to 20) μm. The source is typically a superluminescent diode laser, with a resolution as low as 7 μm. The x axis (Figure 1) spatial resolution of OCT is determined by the focal spot size on the sample which is typically (10 to 30) μm. The ultimate limitation on the depth of penetration within the sample is the attenuation of light caused by scattering. Three-dimensional images of the sample are obtained by rastering the sample in x between successive OCT measurements along the z-axis.

In this work, OCT was used to image an epoxy/unidirectional E-glass composite. The volumetric images were converted to binary and input into a flow code for prediction of axial and transverse permeabilities. The predicted permeabilities of different automated image processing routines are compared with experimental values.

Experimental

Materials

The epoxy resin system consisted of a diglycidyl ether of bisphenol A (DGEBA) monomer (Tactix123, Dow Chemical Company, Midland, MI) and two amines [10]. Aromatic methylene dianiline (MDA) and aliphatic poly(propylene glycol)bis(2-aminopropyl ether) (JeffamineD400) ($M_n \approx 400$) were purchased and used as received from Aldrich (Minneapolis, MN). The oxirane/amine stoichiometry was a mol ratio of 2/1, oxirane/amine. The amine composition that consisted of 0.07 mol MDA and 0.93 mol D400. The refractive index of the composite is 1.55 [11]. The axial length or depth of field is: 4.5 mm/1.55=2.9 mm for image. Details of the mixing and resin transfer molding are provided elsewhere [12].

Experimental Permeability Determination

Details about experimental determination of the axial and transverse permeabilities are provided elsewhere [11].

Instrumentation

Details of the instrumentation are provided elsewhere [13].

Image Processing

Feature Recognition

An automated image processing program was written using MATLAB 5.1 [10] with the Image Processing Toolbox to convert the raw gray scale OCT images to binary images of glass fiber and epoxy. The raw image is first rotated and cropped to eliminate sample tilt and edge effects. The image is then doubled in size by linear interpolation of adjacent pixels to minimize any artificial alteration of the tow size in subsequent image processing.

To increase the contrast between the darker tows and the lighter epoxy regions, a variance image is created by replacing the intensity value of a 2x2 cluster of pixels with the standard deviation of that cluster. Using the automated program, the boundary of the tows are determined and a binary image is formed using thresholding. In the next two steps, spurious "on" pixels within the image and vertical lines corresponding to detector saturation are eliminated. The image is then scaled to the proper aspect ratio and a filling operation is applied to better define the tows. The resulting binary image is then used as input for the permeability calculation.

Level-Set Methods

Level-set methods for image processing were developed by J. Sethian [14] and are a robust method for image de-noising and feature recognition. In short, level-set methods involve the use of a propagating front upon which the speed of propagation at each point along the front is determined by the curvature of the front and the gradient of the image at that point. The curvature dependent portion of the speed makes the front as smooth as possible and eliminates small concave and convex regions (i.e. inlets and peninsulas). The gradient dependant speed allows for fast propagation along areas with small image gradients while pinning the front at areas with high image gradients (i.e. feature boundaries).

Lattice-Boltzman Methods

Details of the lattice-Boltzman computation are provided elsewhere [11].

Results and Discussion

The experimental and calculated axial (K_{ax}) and transverse (K_{tr}) permeabilities are provided in Table 1 for comparison. In Figure 1, the axial permeability would be computed for flow along the y axis. Transverse permeability would be computed for flow along the x axis. K_{ax} is measured or computed for flow along the fiber tows. Image sets for computing K values within this table were processed in two different ways: For the "Manual" method (Figure 1A), the tow outlines were drawn by sight and filled in to generate a binary image. Images using the "Automated" method were processed as described in the experimental section. For Data 2 (Figure 1A, the K_{ax} of 3.81×10^{-4} mm^2 is considered to have the most realistic image processing since the tows are manually traced from the OCT image. Part of the discrepancy between the experimental value for K_{ax} (K_{tr}) and the calculated values may also originate from micro-scale variations of permeability within the fabric. The twenty-one images ((75-95) or (4-24)) used in these calculations represent only a width of 6.0 mm (x axis), a depth of approximately 1.5 mm (z axis), and, most importantly, a length of 1.0 mm (y axis). For comparison, the size of the reinforcement used in experimental determination of permeability is 15 cm wide (x axis, Figure 1), 1.3 cm deep (z axis, Figure 1) and 15 cm long (y axis, Figure 1). The effect of micro-scale variation in the permeability can also be illustrated by comparing K_{ax} from Data 1 and Data 2. The K from Data 1 is 4.45×10^{-4} mm^2 and is calculated using five images (y=0.25 mm), whereas the K from Data 2 is 3.81×10^{-4} mm^2 and is calculated using twenty-one images (y=1.05 mm).

The Brinkman fraction is defined as the fractional area occupied by the tows in the image and naturally varies slightly from image to image. The average Brinkman fraction is shown along with the standard deviation of the image set. The higher the area occupied by the tows (or the higher the Brinkman fraction), the lower K_{ax} and K_{tr} because there is less open space available for fluid flow. If the Brinkman fractions are solely considered, then the K_{ax} for Data 3 (Figure 1B) should be higher than for Data 2 (Figure 1A) since the Brinkman fraction for Data 3 is slightly lower than for Data 2. For the automatically processed images in Data 3, the K_{ax} is in fact lower than for Data 2. In short, a rough tow surface is very effective in suppressing fluid velocity and thus artificially decreases the calculated permeability. From these results, it is evident that improving the smoothness of the tow boundaries is an important next step.

To improve the smoothness of the tow boundaries, a smoothing operation in the form of a binary opening and closing was performed on the automatically processed data. Data 4 from Table 1 shows the resulting permeability and Brinkman fraction of the smoothed data. Upon smoothing, the permeability increases. However, the resulting Brinkman fraction is substantially lower than for the manually processed images. Thus, this particular smoothing operation is considered to be an unsatisfactory procedure for the image data.

The large difference in permeabilities between Data 4 and Data 5 again illustrates the micro-scale variation of permeability within the reinforcement. Again, both image sets represent a 1.05 mm long section of sample. Image set 75-95 is 2.55 mm farther down the sample than image set 4-24. For a rough comparison, image set 4-24 has three images that contain crossing threads while image set 75-95 has 15 images with crossing threads. These crossing threads are processed into the image as connections between the layers of tows. For the permeability calculation, they are assigned the same intrinsic permeability as the glass tows and also act to suppress the fluid flow. It has been shown experimentally that crossing threads have a large influence on decreasing the permeability and that removal of the crossing threads led to as much as a factor of six increase in the experimentally determined permeability when the same fiber volume fractions and packing geometries were compared (15).

The effect of tow roughness on permeability is illustrated when the permeability results from Data 6 (Figure 1C) and Data 7 (Figure 1D) are compared. The images from Data 6 (Figure 1C) are originally from Data 2 (Figure 1A), the manually processed images. However, a small amount of random roughness was introduced in Data 6 while retaining nominally the same Brinkman fraction, leading to an increase in tow surface area. For Data 7, the images in Data 2 were dilated to increase the Brinkman fraction, but the roughness was not altered. When the axial K from Data 7 is compared to Data 6, the result is initially unexpected. A relative increase of roughly 4 % of the Brinkman fraction in Data 7 should lead to a decrease in K_{ax} over Data 6, but the result is the opposite. The K_{ax} of Data 7 is higher than Data 6. This comparison between the permeabilities from Data 6 and Data 7 means that surface roughness is comparable to or more influential than Brinkman fraction in influencing permeability when changes of similar magnitude are compared.

The results of the level-set method for processing the OCT images is shown in Data 8 and in Figure 1E. The computed axial permeability agrees very well with the best possible value in Data 2. In addition, the images were processed with minimal alternation to the tow surface area (roughness) and the Brinkman fraction.

Conclusions

The microstructure of a unidirectional glass-reinforced composite was accurately and rapidly obtained using optical coherence tomography. OCT images were processed and input into a microscale flow model for permeability prediction. It was found that the Brinkman fraction, and the tow surface area generated by the image processing have an important influence on the accuracy of the permeability calculations when compared to the expected values. By using robust image processing methods that maintain the Brinkman fraction and tow surface area, excellent agreement between the calculated and the experimental axial and transverse permeabilities was obtained. However, only a small portion of the composite was sampled. The variability of the permeability throughout the composite still needs to be evaluated on many samples. Only by doing this can a true evaluation of this approach be performed.

References

1. R. Parnas and A. Salem, *Polymer Composites*, **14(5)**, 383(1993).
2. H. Friedman, R. Johnson, B. Miller, D. Salem, and R. Parnas, *Polymer Composites*, **18(5)**, 663(1997).
3. M. Spaid and F. Phelan Jr., *Phys. Fluids*, **9(9)**, 2468 (1997).
4. M. Spaid, and F. Phelan Jr., *Composites: Part A*, **29**, 749, (1998).
5. R. Pitchumani and B. Ramakrishnan, *Int. J. Heat Mass Transfer*, **42(12)**, 2219(1999).
6. S. Ranganathan, R. Easterling, S. Advani, and F. Phelan Jr., *Polymers & Polymer Composites*, **6(2)**, 63, (1998).
7. D. Huang, E. Swanson, C. Lin, J. Schuman, W. Stinson, W. Chang, M. Hee, T. Flotte, K. Gregory, C. Puliafito, and J. Fujimoto, *Science*, **254**, 1178, (1991).
8. J. Fujimoto, M. Brezinski, G. Tearney, S. Boppart, B. Bouma, M. Hee, J. Southern, and E. Swanson, *Nature Medicine*, **1**, 970, (1995).
9. M. Bashkansky, M. Duncan, M. Kahn, D. Lewis, J. Reintjes, *Opt. Lett.*, **22**, 61(1997).
10. Identification of a commercial product is made only to facilitate experimental reproducibility and to adequately describe experimental procedure. In no case does it imply endorsement by NIST or imply that it is necessarily the best product for the experimental procedure.
11. J. Dunkers, F. Phelan, C. Zimba, K. Flynn, R. Peterson, R. Parnas, R. Prasankumar and J. Fujimoto, *Proc. ANTEC*, 1999.
12. J. Dunkers, R. Parnas, C. Zimba, R. Peterson, K. Flynn, J. Fujimoto, and B. Bouma, *Composites, Part A*, **39**, 139(1999).
13. J. Dunkers, F. Phelan, C. Zimba, K. Flynn, D. Sanders, R. Peterson, R. Parnas, X. Li and J. Fujimoto, *Proc. of SPE ANTEC*, 1999.
14. J. A. Sethian, "Level Set Methods and Fast Marching Methods", Cambridge University Press, 1999.
15. F. Phelan, Jr., Y. Leung and R. Parnas, *J. Therm. Comp. Mat.*, **7**, 208(1994).

Sample Name	Type of Processing	Image Set	Axial K x 10^{-4} (mm^2)	Transverse K x 10^{-4} (mm^2)	Anisotropy Ratio	Brinkman Fraction
Experimental	N/A	N/A	5.3±2.6*	0.750	7.07	0.770
Data 1	Manual	87-91	4.45	0.882	5.05	0.767
Data 2	Manual	75-95	3.81	0.992	3.84	0.788±0.021
Data 3	Automated No Smoothing	75-95	2.83	0.654	4.32	0.768±0.021
Data 4	Automated Smoothing	75-95	3.18	0.991	3.21	0.750±0.027
Data 5	Automated Smoothing	4-24	5.09	0.934	5.45	0.727±0.014
Data 6	Manual Roughened	75-95	2.73	0.662	4.12	0.795±0.021
Data 7	Manual Dilated	75-95	2.99	0.767	3.90	0.837±0.020
Data 8	Level-Set	75-95	3.68	0.997	3.69	0.778+0.032

Table 1: Experimental and calculated values for axial (K_{ax}) and transverse (K_{tr}) permeability and Brinkman fraction.
*This error is the standard deviation or standard uncertainty of the four saturated flow measurements.

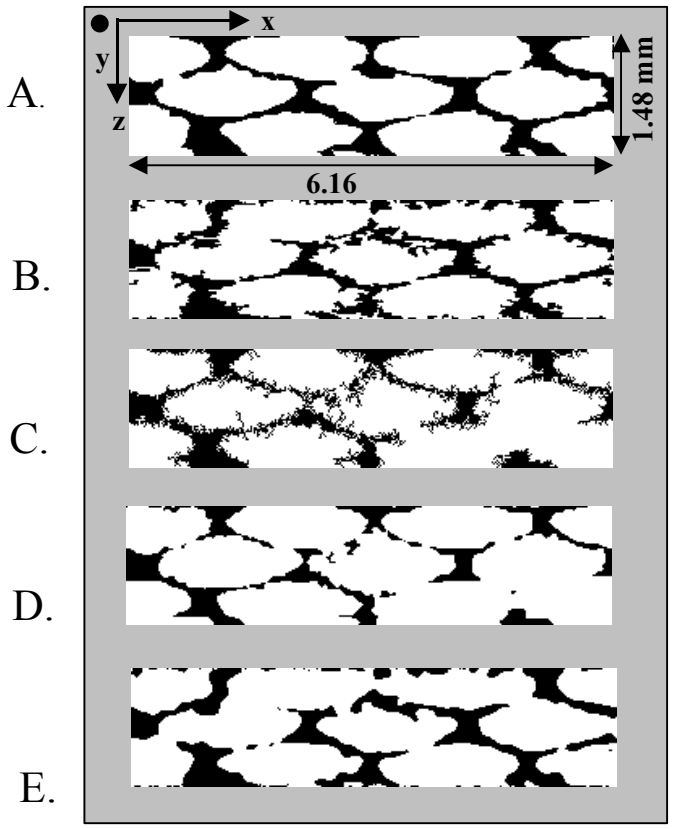

Figure 1: Binary images resulting from different image processing techniques for image slice 75. Manually processed image. (A), Automatically processed image (B.), Manually processed image in A. with added random roughness (C.), Manually processed image in A. with tow dilation (D.), Level-set processed image (E.).